PERGAMON

International Journal of Heat and Mass Transfer 45 (2002) 1237–1248

International Journal of HEAT and MASS TRANSFER

www.elsevier.com/locate/ijhmt

A numerical study of the unsteady flow and heat transfer in a transitional confined slot jet impinging on an isothermal surface

Victor A. Chiriac, Alfonso Ortega *

Department of Aerospace and Mechanical Engineering, University of Arizona, Aero Building 119, Room 614, P.O. Box 201119, Tucson, AZ 85721-0119, USA

Received 11 May 2000; received in revised form 30 June 2001

Abstract

A numerical finite-difference approach was used to compute the steady and unsteady flow and heat transfer due to a confined two-dimensional slot jet impinging on an isothermal plate. The jet Reynolds number was varied from $Re = 250$ to 750 for a Prandtl number of 0.7 and a fixed jet-to-plate spacing of $H/W = 5$. The flow was found to become unsteady at a Reynolds number between 585 and 610. In the steady regime, the stagnation Nusselt number increased monotonically with Reynolds number, and the distribution of heat transfer in the wall jet region was influenced by flow separation caused by re-entrainment of the spent flow back into the jet. At a supercritical Reynolds number of 750 the flow was unsteady and the net effect in the time mean was that the area-averaged heat transfer coefficient was higher compared to what it would have been in the absence of jet unsteady effects. The unsteady jet exhibited a dominant frequency that corresponded to the formation of shear layer vortices at the jet exit. Asymmetry in the formation of the vortex sheets caused deformation or buckling of the jet that induced a low-frequency lateral jet "flapping" instability. The heat transfer responds to both effects and leads to a broadening of the cooled area. © 2002 Elsevier Science Ltd. All rights reserved.

1. Introduction

Impinging jets are used in many industrial applications because they produce high transfer coefficients with relatively low pressure drops. Applications include drying of papers and films, tempering of glass and metal during processing, cooling of gas turbine surfaces, and cooling of electronic components. In many industrial applications, such as in cooling of electronics or internal cooling of turbine blade/vane surfaces, the jet outflow is often confined between the target surface and an opposing surface in which the jet orifice is located. The presence of a confining top surface in jet impingement results in a complicated flow in which the free jet behavior is coupled to the behavior of the fluid in the channel formed between the two surfaces. Most previous research has focused on the heat transfer and fluid mechanics in free impinging jets, primarily in the turbulent regime. In microelectronics cooling, air velocities are often limited by acoustic concerns and, hence, impinging jet heat transfer in the turbulent regime may be impractical. From both a fundamental and practical perspective then, both the laminar and turbulent regimes are relevant for investigation. The confined impinging jet provides a practical solution to the microelectronics cooling problem because of the concentration of intense cooling over small areas. It seems reasonable to assume that cooling technology will follow the same path as the electronics, toward miniaturization and integration. For this reason, the potential emergence of milli-scale impinging jets as cooling solutions requires an understanding of the detailed behavior so that it can be scaled downward in physical length scales.

Because of its importance, heat transfer between single or multiple impinging air or liquid jets and a flat surface

* Corresponding author. Tel.: +1-520-621-6787; fax: +1-520-621-8191.

E-mail address: ortega@u.arizona.edu (A. Ortega).

0017-9310/02/$ - see front matter © 2002 Elsevier Science Ltd. All rights reserved.
PII: S0017-9310(01)00224-1

Nomenclature

C_f	friction coefficient $(\tau_w/\frac{1}{2}\rho V_j^2)$
C_p	pressure coefficient $[(p_x - p_j)/\frac{1}{2}\rho V_j^2]$
f	frequency (s^{-1})
h	heat transfer coefficient $[q/(T_w - T_j)]$
H	nozzle–plate spacing (m)
k	thermal conductivity (W/m K)
L	channel length (m)
Nu_m	local time-averaged Nusselt number based on jet hydraulic diameter $(h2W/k)$
Nu_x	local instantaneous Nusselt number based on jet hydraulic diameter $(h2W/k)$
p	static pressure (Pa)
Pr	Prandtl number (v/α)
q	heat flux at target wall (W/m^2)
Re	Reynolds number based on hydraulic diameter $(2WV_j/v)$
S	source term in general equation
t	time (s)
T	temperature (K)
u	velocity in jet transverse direction (m/s)
v	velocity in jet streamwise direction (m/s)
V_j	jet inlet velocity (m/s)
W	jet nozzle width (m)
x	jet transverse coordinate (m)
y	jet streamwise coordinate (m)

Greek symbols

α	fluid thermal diffusivity (m^2/s)
∇	div/del operator
ϕ	dependent variable in general equation
Γ	diffusion coefficient in general equation
v	kinematic viscosity (m^2/s)
ρ	density (kg/m^3)
τ_w	wall shear stress (N/m^2)

Subscripts

j	jet
stag	stagnation
w	target wall
x	local value of parameter on target wall

has been the subject of numerous investigations over the last four decades, most of them experimental. Lytle and Webb [1] experimentally investigated the impingement of a circular air jet on a flat plate for nozzle-to-plate spacings of less than one nozzle diameter and Reynolds numbers varying from 3600 to 27 600. They found that, for H/d of less than 0.25, the maximum local heat transfer did not occur at the stagnation point but at a radial (r) location that depended on Reynolds number and nozzle-to-plate distance, d. A local minimum heat transfer developed at the stagnation ($r = 0$) point and two distinct peaks were observed in the radial direction. The first peak in the Nusselt number occurred in an annular region around $r/d = 0.5$, due to the non-uniform, mixing-induced turbulence in the developing jet. The second peak occurred in the region $1.5 < r/d < 2.5$, as a result of the retransition of the wall jet from laminar to turbulent.

Huang and El-Genk [2] investigated the heat transfer between a uniformly heated flat plate and a circular impinging jet. In their experiments, Re was varied from 6000 to 60 000, the radial distance from the stagnation point from 0 to 10 cm, and the nozzle-to-plate spacing, H, from 1 to 12 cm. For all Reynolds numbers and $H \geqslant 2$ cm, the lowest wall temperature always occurred at the stagnation point ($r = 0$). At smaller spacings ($H \leqslant 1$ cm) and $Re > 13\,000$, the maximum Nu still occurred at the stagnation point. However, for lower Reynolds numbers, its location shifted outward to $r/d = 1.8$–2.0 as Re was increased.

The influence of vortices on the thermal field of the jets was investigated experimentally by Kurosaka et al. [3]. When a thermally insulated flat plate was inserted into an impinging jet, the wall temperature distribution was modified by the presence of a secondary layer of vortices imposed on the plate by the primary vortex ring of the jet. When the plate was near the jet nozzle, a region of lower wall temperatures was observed as a result of the additional vortices. When placed farther from the jet nozzle, the secondary vortices were not present in the flow and the region of lowered wall temperatures vanished.

Anderson et al. [4] experimentally investigated stagnation zone flow in impinging jets. Small particles of glass beads were injected into air impinging jets at flow Reynolds numbers of 21 000. Particle velocities near the wall deviated strongly from fluid velocities, resulting in rebound. The deceleration associated with the rebound caused a significant increase in particle density above the impinging plate in the stagnation region. The shear layer vortices induced spatial variations in the particle concentration in the free jet, causing time fluctuations in the particle number density near the plate. Collisions with the plate were nearly elastic, with particles rebounding strongly into the impinging flow. Particles gained radial velocity near the peaks of their rebound trajectories at locations where their residence times were longest. Furthermore, in order to capture the particle–vortex interactions, the jet was acoustically forced at a frequency of 180 Hz, corresponding to the naturally occurring harmonic for the flow. Cross-sectional images showed that the free jet vortices produced spatial variations in the particle concentrations, causing temporal

fluctuations in the density of particles in the stagnation zone.

The presence of a confining top plate facing the target plate in jet impingement results in a more complicated flow structure and only recently have studies focused on this configuration. Fitzgerald and Garimella [5] experimentally investigated the flow field of an axisymmetric, confined, submerged, turbulent jet impinging normally on a flat plate. Reynolds numbers varied from 8500 to 23 000. Flow field measurements proved that, in the potential core of the air jet, the confinement increased the length of the core, decreased turbulence levels in the jet, and reduced the heat transfer at the stagnation point by up to 10% in comparison to the free jet. A recirculation zone was observed moving radially outward from the stagnation zone, with an increase in both Reynolds number and nozzle-to-plate spacing.

Garimella and Rice [6] investigated the heat transfer from a small heat source to a normally impinging axisymmetric and submerged liquid jet in confined and unconfined configurations for electronics cooling situations. The nozzle diameter ($0.79 \leqslant d \leqslant 6.35$ mm), Reynolds number (4000–23 000), and nozzle-to-source spacing ($1 \leqslant H/d \leqslant 14$) were all varied. For a given H/d and Re, the smaller nozzles generally produced the higher heat transfer coefficients, especially in the stagnation region where the heat transfer coefficient for the 0.79 mm nozzle was 3.5 times greater than that for the 6.35 mm nozzle. The stagnation and area-averaged heat transfer coefficients increased with increasing Reynolds number. Secondary peaks, resulting from the transition to turbulence in the wall jet region, were noted in the local distributions around $r/d = 2$. In some cases, the heat transfer coefficients for the secondary peak were higher in magnitude than those at the stagnation point.

Morris and Garimella [7] used a commercial finite-volume code to investigate the local heat transfer coefficient distribution on a square heat source due to a normally impinging, axisymmetric, confined, and submerged turbulent liquid jet. Numerical predictions were made for nozzle diameters of 3.18 and 6.35 mm at several nozzle-to-heat source spacings and the Reynolds number varied from 8500 to 13 000. The results showed good agreement, 16–20% accuracy, with experiments.

A review of the literature has revealed that the behavior of the two-dimensional impinging jet in the laminar and transitional regime is not at all well known. Principally, this is because most studies have been motivated by the industrial use of impinging jets with macro-scale dimensions, of order 1 cm and greater. If we consider the potential use of impinging jets at increasingly smaller scales, from milli-scale to even micro-scale, practical limitations will clearly limit their operation to the laminar regime. Hence, the objectives of the present study are to characterize the behavior of the confined laminar impinging jet and the attendant heat transfer removal to the target wall. Since the stability of this fundamental flow is not well documented, particular attention is paid to identifying transitions to unsteady regimes and their effects on the heat transfer.

2. Problem description

The problem geometry and nomenclature are shown in Fig. 1. A two-dimensional jet with uniform velocity V_j enters from a nozzle of width W into a channel with height H and length L, for a fixed geometry of $H/W = 5$ and $L/W = 25$. The jet Reynolds number, based on a hydraulic diameter of $2W$, is varied from 250 to 750. The Prandtl number is assumed to be 0.72, with air as the cooling fluid. The upper confining wall at $y = 0$ is adiabatic while the lower target wall at $y = H$ is isothermal at T_w. The temperature of the target wall is maintained at 10 K above the temperature of the entering jet, T_j. The following physical parameter values were used for all of the present calculations: $W = 1$ cm, $H = 5$ cm, $L = 25$ cm, $V_j = 0.2$–0.6 m/s.

The flow is assumed to be two-dimensional, unsteady, non-isothermal, incompressible, and laminar in a Cartesian reference frame. The fluid density, viscosity, and thermal conductivity are assumed to be constant. Viscous dissipation effects are neglected in the energy equation. With these simplifications, the continuity, two-dimensional momentum, and energy equations are written in vector form as

$$\nabla \cdot \bar{u} = 0, \tag{1}$$

$$\frac{\partial \bar{u}}{\partial t} + \bar{u} \cdot \nabla \bar{u} = -\frac{1}{\rho}\nabla p + \nu \nabla^2 \bar{u}, \tag{2}$$

$$\frac{\partial T}{\partial t} + \bar{u} \cdot \nabla T = \alpha \nabla^2 T. \tag{3}$$

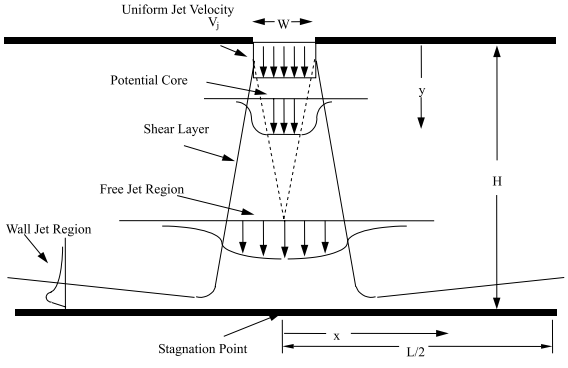

Fig. 1. The geometry of a two-dimensional confined impinging jet.

The boundary conditions are as follows:

On the upper plate:

$$y = 0, \quad -\frac{W}{2} \leqslant x \leqslant \frac{W}{2}, \quad v = V_j, \quad u = 0, \quad T = T_j,$$
$$y = 0, \quad \frac{W}{2} \leqslant x \leqslant L, \quad v = 0, \quad u = 0, \quad \frac{dT}{dy} = 0, \tag{4}$$
$$y = 0, \quad -L \leqslant x \leqslant -\frac{W}{2}, \quad v = 0, \quad u = 0, \quad \frac{dT}{dy} = 0.$$

On the lower plate:

$$y = H, \quad -\frac{L}{2} \leqslant x \leqslant \frac{L}{2}, \quad v = 0, \quad u = 0, \quad T = T_w. \tag{5}$$

At the ends of the channel:

$$x = \pm L, \quad \frac{du}{dx} = 0, \quad \frac{dv}{dx} = 0, \quad \frac{dT}{dx} = 0. \tag{6}$$

The actual computational domain consisted of the entire channel, L in length and H in height, since asymmetric, unsteady solutions were expected.

3. Numerical procedure

The numerical calculations were performed using the fluid and heat transfer solver (FAHTSO) code, a custom CFD/CHT solver developed for solving the momentum and energy equations in two- or three-dimensional steady or unsteady flows. A brief description of the numerical procedure is presented here. Complete information can be found in [8,9].

The discretized equations are derived from the differential equations by using a finite-volume discretization procedure. Eqs. (1)–(3) can be represented by a general differential equation as follows [10]:

$$\frac{\partial}{\partial t}(\rho\phi) + \mathrm{div}(\rho\bar{u}\phi) = \mathrm{div}(\Gamma\,\mathrm{grad}\,\phi) + S, \tag{7}$$

where the values for the ϕ, Γ, and S are given in Patankar [10], for example.

The generalized equation, Eq. (7), is discretized in time and space in precisely the same manner for all the dependent variables. Time discretization uses a second-order Euler method. The second-order diffusion terms are discretized using a second-order central-difference formulation, and the convective terms are discretized using the QUICK scheme [11]. The expressions for the velocity equations are fully implicit in the SIMPLE algorithm, therefore, the summation terms for the neighboring velocities are omitted and a pressure correction formula is added. The equations are solved using an iterative procedure on a staggered grid.

A systematic grid resolution study was performed. A non-uniform grid was used in both directions. The grid was separated into three separate regions in both the x- and y-directions. Three grid structures were considered: 60×44, 84×62, and 116×86, where the numbers are the number of grids in the x- and y-directions, respectively. The grid nodes were appropriately refined near the wall surface and jet shear layer in order to capture the large gradients. The grid ratios between the adjacent grid structures were between 0.8 and 1.2, and the clustering parameters were set to produce a uniform change in the grid spacing. The results of the grid resolution study indicated that the 84×62 grid adequately captured the physics of the flow. A complementary time-step independence study was performed for the unsteady flows. Five time steps were investigated: $t = 0.5 \times 10^{-4}$, 0.8×10^{-4}, 0.1×10^{-3}, 0.125×10^{-3}, and 0.25×10^{-3} s. The primary criterion in choosing the time step was adequate resolution of the frequency spectra and the root-mean-square values for the velocities investigated at three monitoring locations in the flow. A time step of $t = 0.1 \times 10^{-3}$ s was found to be adequate. All numerical calculations were performed on an SGI Origin 2000 system at The University of Arizona. The actual CPU time was neither determined for any of the runs nor was it considered particularly relevant.

4. Results and discussion

4.1. Steady laminar regime

Fig. 2 illustrates typical velocity fields for subcritical, steady Reynolds numbers of 250 and 500, and Fig. 3 gives the respective temperature contours. As is typical of impinging jets, the flow undergoes severe acceleration as it turns and then evolves into a plane wall jet. For a Reynolds number of 250 (Fig. 2(a)), the flow separates from the impinging plate. The jet momentum at this Reynolds number is not able to overcome the opposing frictional forces of the wall and the retarding effects of the entrained flow in the upper part of the channel. As a result, the flow decelerates and separates. At $Re = 500$ (Fig. 2(b)), no separation of the impinging wall occurs, but the jet entrainment induces a weak backflow into the channel at the channel exit. The thermal diffusion layer (Fig. 3) is clearly thinnest at the stagnation point, and its thickness grows rapidly as the normal component of the velocity diminishes in the wall jet region. Both the temperature and velocity fields in the stagnation region indicate a steady, symmetrical flow.

Comparisons of the instantaneous wall pressure, friction, and heat transfer coefficients at Reynolds numbers of 250 and 500 are shown in Figs. 4–6, respectively. As expected, the highest values are obtained at the stagnation point. Inspection of the pressure coefficients in Fig. 4 reveals that $C_p = 1.0$ for $Re = 500$, indicating that, for all practical purposes, the jet core with V_j velocity impinges on the plate. Recovery of nearly 100% of the total jet pressure is achieved at the stagnation point. The wall static pressure drops rapidly

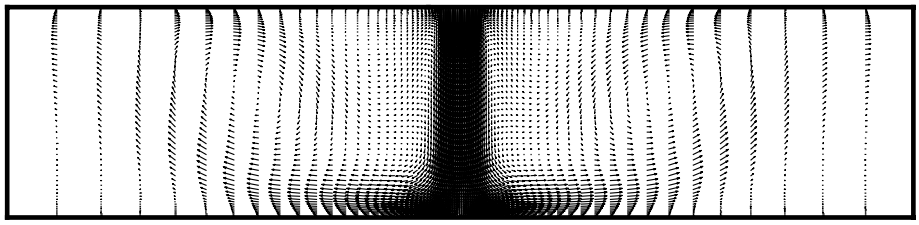

(a)

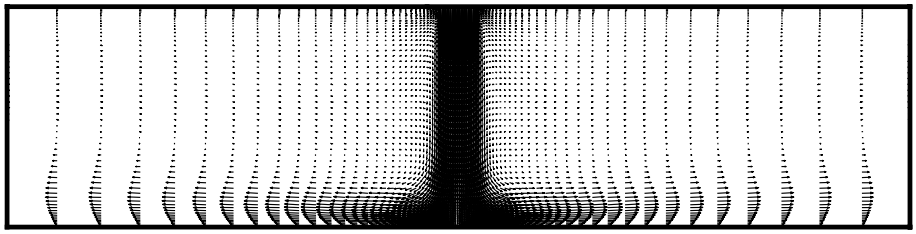

(b)

Fig. 2. Velocity fields for the confined impinging jet in the steady regime: (a) $Re = 250$; (b) $Re = 500$.

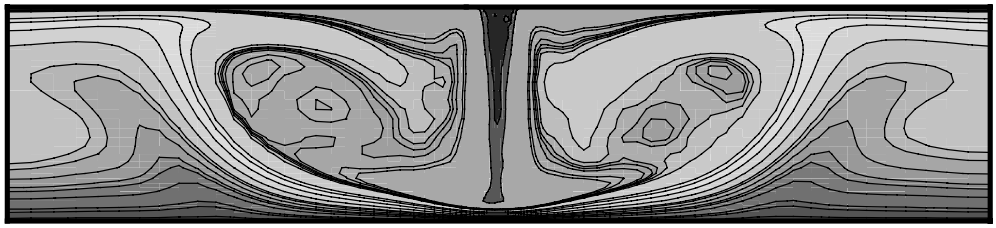

(a)

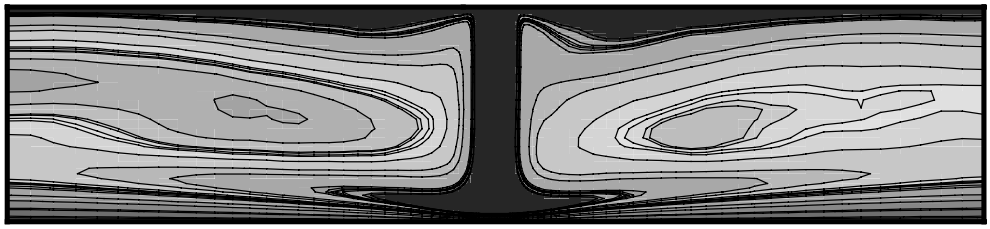

(b)

Fig. 3. Temperature contours for the confined impinging jet in the steady regime: (a) $Re = 250$; (b) $Re = 500$.

as the flow turns and accelerates. At $Re = 250$, viscous effects are clearly more dominant, leading to a higher jet growth rate and hence a decrease in the normal jet velocity impinging at the stagnation point. This leads to the observed drop in the stagnation pressure, noting that C_p is normalized on the initial jet velocity. The mild pressure recovery in the wall jet region at $Re = 250$ is caused by a flow separation that is induced by the adverse pressure gradient introduced by the tendency for the spent flow to be re-entrained by the jet. Note that this re-entrainment is a distinct feature of the confined jet. At both Reynolds numbers, the wall shear stress rapidly increases away from the stagnation point as the stagnation point flow evolves to a parallel wall jet (Fig. 5). The rapid increase in strain maximizes and then diminishes monotonically as the wall jet develops. For the case of $Re = 250$, the wall shear stress nearly vanishes due to the flow separation.

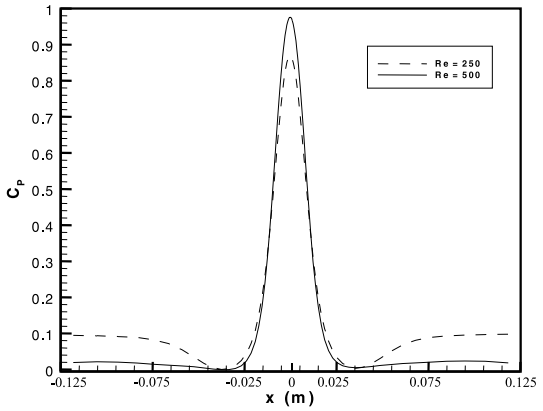

Fig. 4. Wall pressure coefficients in the steady regime.

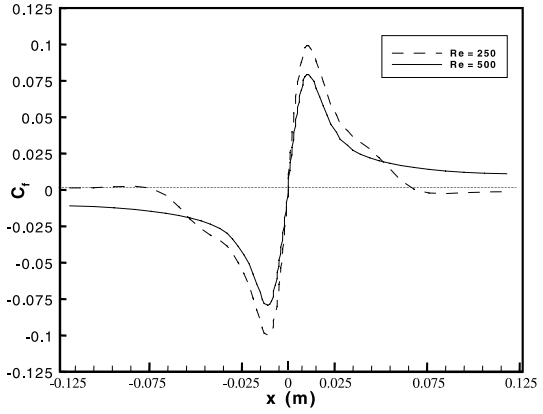

Fig. 5. Wall friction coefficients in the steady regime.

The convective heat transfer from the impingement wall is consistent with observations of the momentum transport (Fig. 6). For subcritical Reynolds numbers of 250 and 500, the time-averaged Nusselt number on the wall peaks at the stagnation point, in direct proportion to the thickness of the thermal boundary layer. At $Re = 500$, the local time-averaged Nusselt number decays monotonically. The initial decay rate is rapid in the region where the normal velocity turns aggressively to a parallel velocity in the wall jet. The decay rate then decreases in the wall jet region. Similarly, for $Re = 250$, the stagnation Nusselt number is lower due to the thicker diffusion layer, but the decay rate is also lower since the arriving jet is broader in the transverse direction. In addition, Nu diminishes to a value of about 0.75, less than for $Re = 500$, due to the flow separation.

The time-averaged Nu for $Re = 750$ demonstrates behavior that is, in several ways, indicative of a shift in the flow region. The peak value is higher, but the rate of decay of Nu away from the stagnation point shows an inflection point that broadens the effectively cooled area. However, Nu decays to a low value in the parallel flow region, again pointing to the flow separation as the likely cause. The more detailed examination discussed in the following section shows that $Re = 750$ represents a supercritical regime in which a periodic unsteady flow is encountered. Fig. 7 shows the time-averaged Nusselt number at the stagnation line, Nu_{stag}. Up to $Re \approx 650$, Nu_{stag} scales with $0.6Re^{0.5}$, consistent with the calculations of Wheeler and Neti [12] shown for comparison. Departure from this steady regime is evidenced by the change in slope above $Re = 650$. Previously, this unsteady transition has not been noted. At increasing Re, the unsteady laminar regime will give way to further transition to a fully turbulent regime, but mapping this

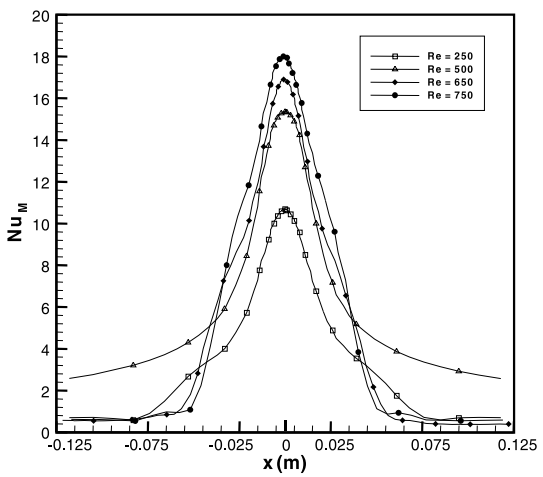

Fig. 6. Local time-averaged Nusselt numbers on impingement wall.

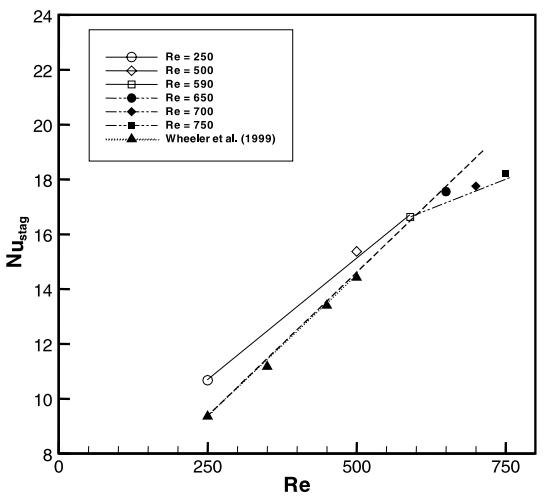

Fig. 7. Time-averaged stagnation Nusselt number versus Reynolds number.

latter stage of transition is beyond the scope of this paper.

4.2. Unsteady laminar regime

For $Re > 650$, the flow is unsteady, as seen in the representative velocity fields given in Fig. 8 for $Re = 750$. The symmetry of the flow is disrupted and highly unsteady effects are observed. The jet core is distorted, and vortices are alternately shed on both sides of the jet. Aggressive flow entrainment causes the wall jet flow to be partially re-entrained into the jet, causing the wall jet flow to separate and form a pair of recirculating zones. Recall that, in the absence of unsteadiness, separation occurred at $Re = 250$ but not at 500. Interestingly, the detached wall jet flow is almost completely re-entrained; the mass efflux observed at the upper half of the channel exit is partly jet fluid and partly backflow into the channel. From the point of view of removing heat or mass from the target wall, this aggressive re-entrainment is detrimental, hence, it is not immediately obvious whether unsteadiness is beneficial or detrimental overall.

In order to quantify the flow instabilities, the velocities were sampled over time at three sampling locations at the jet centerline, $x/H = 0$: $y/H = 0.21$ (near the jet exit), 0.5 (at the mid-channel), and 0.93 (near the target plate). Fig. 9 shows the spectral distribution of the velocity in the jet streamwise direction, y (the v component), and in the jet transverse direction, x (the u component). At the jet exit, Figs. 9(a) and (b), the streamwise velocity component demonstrates a distinct

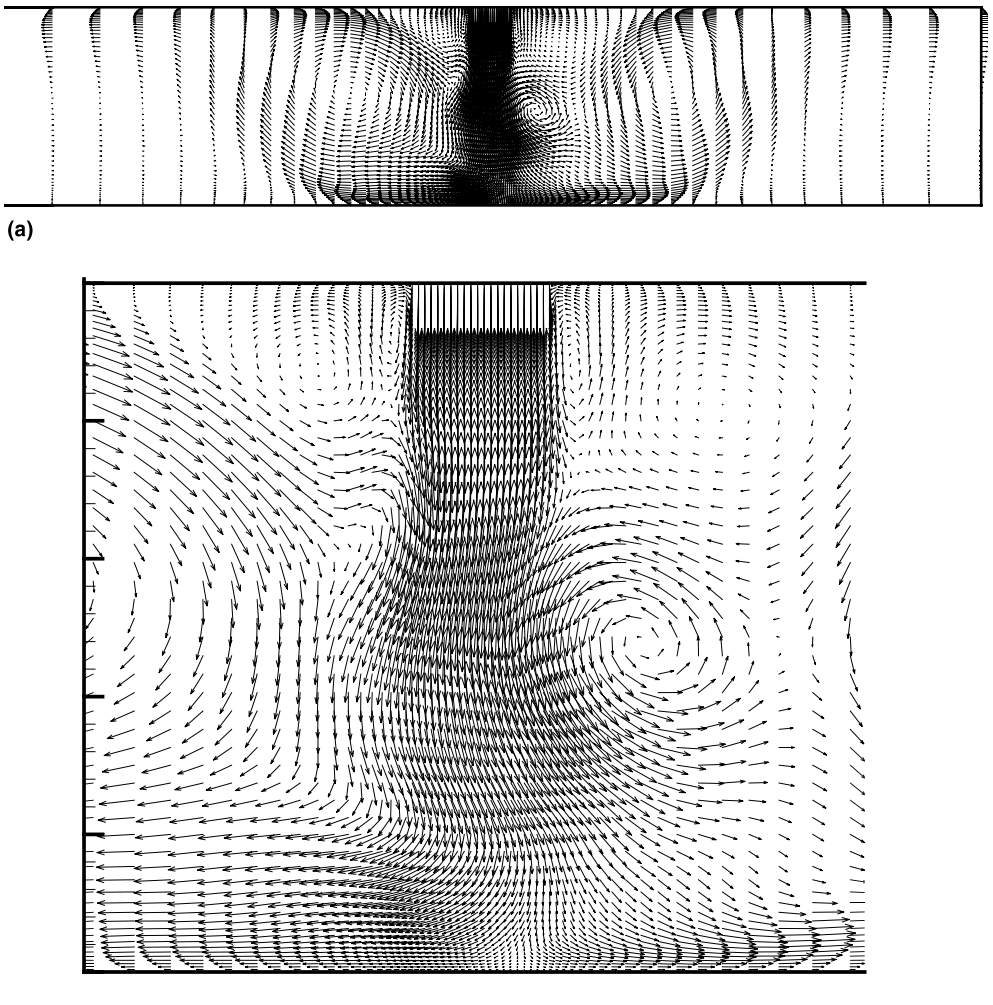

Fig. 8. Velocity fields for the confined impinging jet at $Re = 750$: (a) instantaneous velocities in channel; (b) instantaneous velocities in stagnation region.

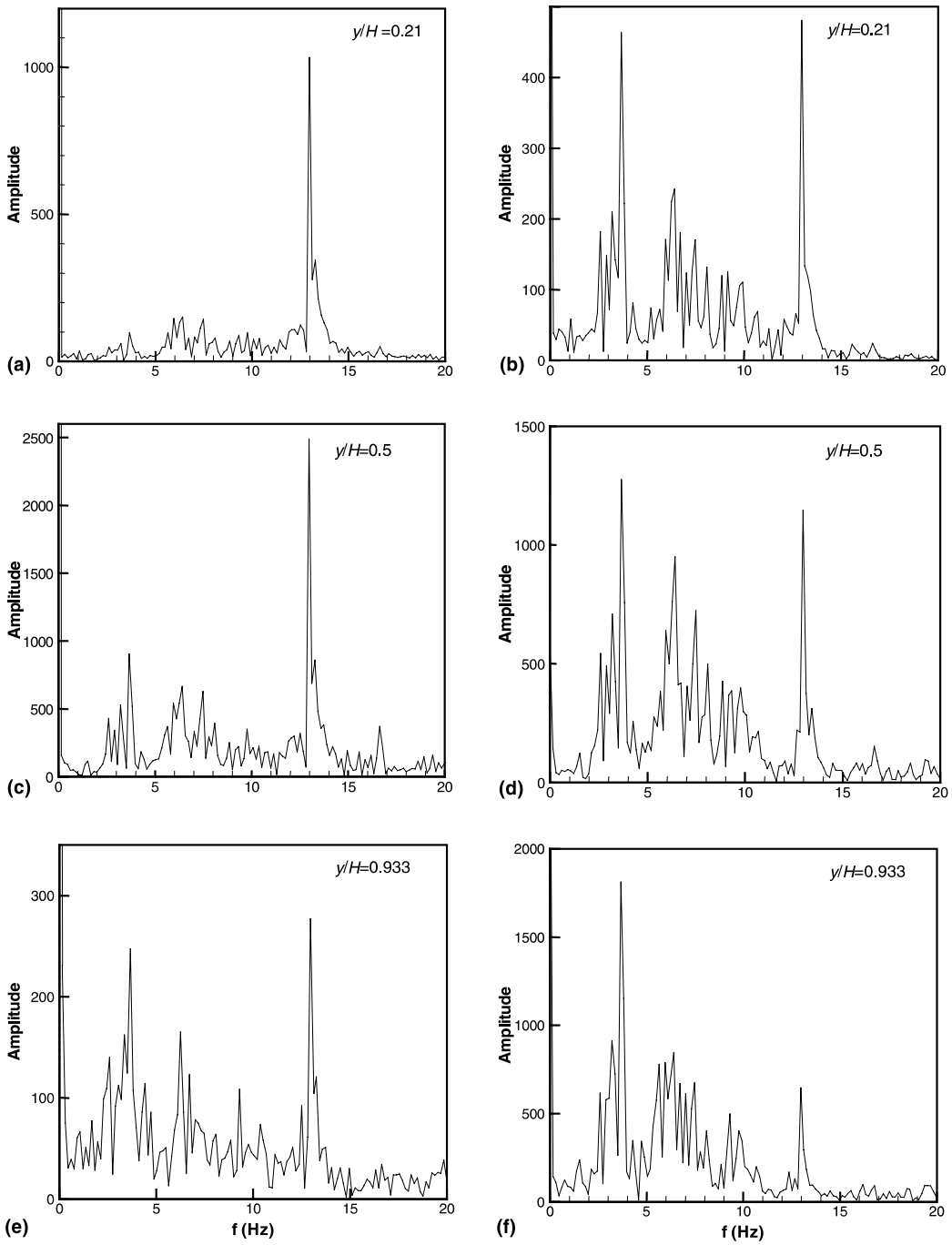

Fig. 9. Frequency spectra for v-velocity [jet streamwise; (a), (c), (e)] and u-velocity [jet transverse; (b), (d), (f)] at three monitoring points at the jet centerline, $x/H = 0$. Note variation in the ordinate scales.

spectral peak at about 13 Hz whereas the transverse component demonstrates dominant frequencies at 3.66, 6.6, and 13 Hz. For $Re = 750$, the jet velocity was $V_j = 0.596$ m/s, hence the characteristic frequency is $V_j/H = 11.92$ Hz. The dimensionless frequencies, or Strouhal numbers (fH/V_j), are 0.31, 0.55, and 1.1, respectively. At the channel mid-plane, the amplitude of the oscillations in both the streamwise (Fig. 9(c)) and

transverse (Fig. 9(d)) components is amplified. (Note that the vertical scales are not fixed.) Nearest to the wall, the amplitudes of the oscillations of the jet streamwise velocity (i.e., the velocity normal to the plate) are damped (Fig. 9(e)). The transverse component (i.e., parallel to the wall) shows that the high frequency (13 Hz) component is greatly damped whereas the 3.66 Hz component is highly amplified (Fig. 9(f)).

In order to clarify the confined jet behavior, a time sequence of the vorticity field is presented in Fig. 10. The figure depicts instantaneous snapshots taken at intervals of 0.05 s, capturing roughly one cycle of the lowest frequency periodic motion. The first figure (Fig. 10(a)) clearly shows four vortices dominating the flow field. Vortex 1 is in the process of being formed, whereas 2, 3, and 4 have been advected downstream toward the target wall. Because of the aysmmetric vortex formation, i.e., alternating on either side of the jet inlet, the vortices in mid-flight are unopposed by a matching vortex on the opposite side of the jet centerline. The vortex circulation induces the jet toward the vortex because of a locally unbalanced pressure field, causing the jet to deflect. These dynamics are well illustrated in Figs. 10(a)–(c). Vortex 2 has caused a deflection to the left whereas Vortex 3 has deflected the jet to the right, leading to what is most aptly described as jet "buckling". With reference to the spectra shown in Fig. 9, it is apparent that the highest frequency harmonic, corresponding to $St = 1.1$, is associated with the frequency at which vortices are formed in the shear layer at the jet exit. Vortex formation alternates from one side to the other, causing jet deflection or buckling at each event.

With reference to the pictorial representation in Fig. 11, the maximum (vortex formation) frequency is related to the buckling wavelength λ shown in Fig. 11 by

$$f_{\max} = \frac{V_j}{\lambda/2}.$$

One half of this maximum frequency would correspond to the passage of a vortex pair and thus is a simple subharmonic of the same phenomena. Because a pair of vortices causes the lateral deflection of the jet centerline from one extreme to the other and back, a stationary observation at the channel mid-height and jet centerline ($x = 0$), Fig. 9(d), detects the passage of each vortex (12.96 Hz). The buckling cycle requires the vortex pair and, hence, is detected at one-half of the dominant frequency (6.6 Hz), as clearly seen in Fig. 9.

The characteristic frequency for the jet/channel combination is $f_{\text{char}} = V_j/H = 11.92$ Hz. The fact that the dominant vortex shedding mode is higher (12.96 Hz), leading to $St = 1.1$, indicates that Vortex 1 is formed and shed before the vortex previously shed from the opposite side (Vortex 2) reaches the impinging wall. With respect to Fig. 11, this means that the "buckling" wavelength λ is slightly less than the channel height H.

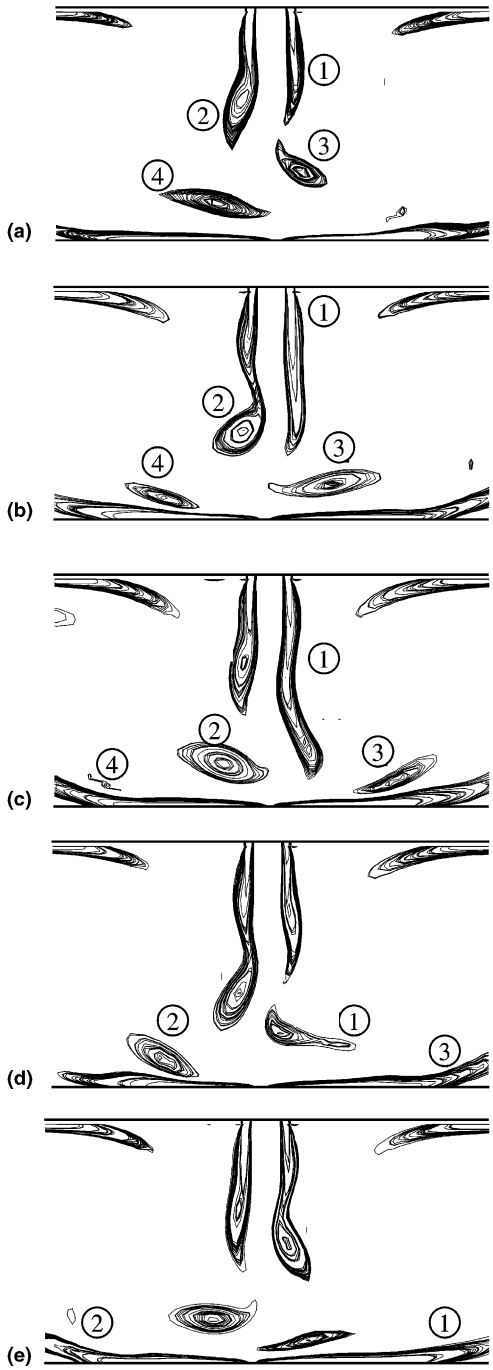

Fig. 10. Time sequence of vorticity contours (ω_z) for $Re = 750$.

The most obvious interpretation is that the edge vortex formation is not simply locked-in by a pressure feedback to the jet exit resulting from the perturbation of the vortex arriving at the target wall. Other, probably nonlinear, mechanisms also contribute.

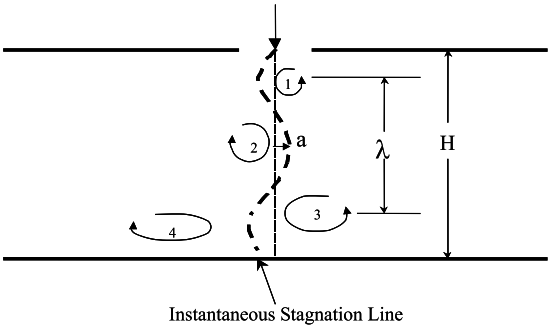

Fig. 11. Pictorial of jet vortex dynamics.

Perhaps most relevant to the convective heat transfer is the fact that the lowest frequency mode (3.66 Hz) is of comparable magnitude to the principal high frequency mode nearest to the target wall, Fig. 9(e), and yet is not a simple subharmonic. Fig. 9(f) shows that the transverse velocity component, i.e., the component parallel to the wall at the stagnation region, is dominated by the lowest frequency mode. To examine this further, Fig. 12 illustrates the oscillations in the x-location of the position of the instantaneous peak static pressure on the target wall. If this location is used to define the instantaneous stagnation line, it becomes clear from Fig. 12 that the stagnation point of the impinging jet oscillates periodically, with a frequency of 3.66 Hz. Fig. 13 compares an instantaneous static pressure distribution to the time mean, illustrating the lateral shift in the entire profile. These data confirm that the lowest frequency mode corresponds to a high-amplitude periodic lateral "flapping" jet motion. Correlation of the periodic flapping cycle demonstrated in Fig. 12 with the vorticity field plot of Fig. 10 shows that between three and four coherent vortices are involved in one "flapping" cycle; these are

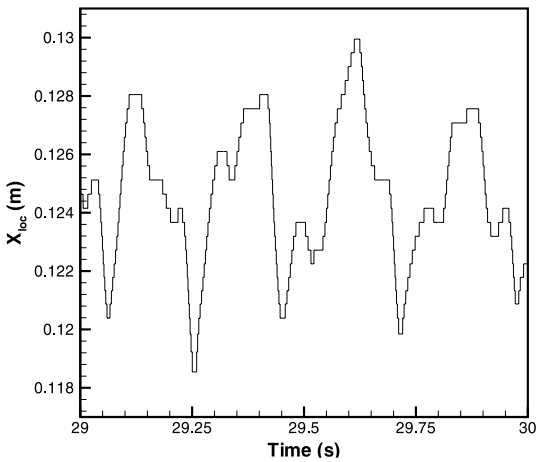

Fig. 12. Variation over 1 s of the location of instantaneous peak pressure.

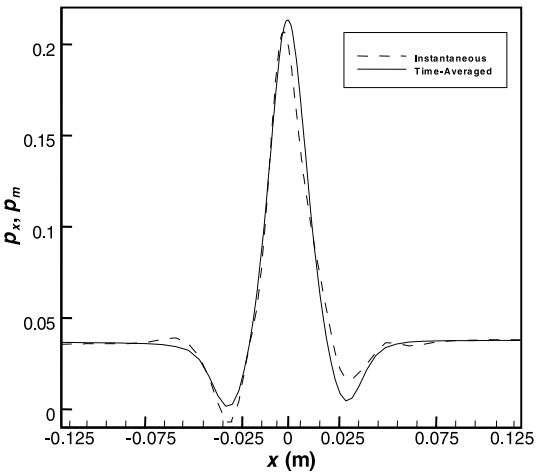

Fig. 13. Time-averaged and instantaneous pressures for $Re = 750$.

readily distinguishable in Fig. 10(a). At a flapping frequency of 3.66 cycles per second, roughly 13 vortices are formed, as confirmed by the dominant vortex shedding frequency of 12.96 Hz. That the jet flapping leads to the large-amplitude stagnation point displacement is easily confirmed with the aid of Fig. 11. If the stagnation line displacement was due solely to the "buckling" of the jet column, the stagnation line would oscillate with a frequency of V_j/λ (which would correspond to 6.6 Hz for $Re = 750$) and the displacement would correspond to the buckling amplitude "a" in Fig. 11. But Fig. 12 clearly points out that the stagnation line oscillates at 3.66 Hz, apparently as a result of jet flapping. We speculate that the flapping instability involves a complicated non-linear coupling between the jet vortex formation and the fluid in the channel. This complex interaction merits further investigation.

The convective wall heat transfer from the supercritical impinging jet responds to the interaction of the shear layer vortices with the wall, apparently at the higher frequencies, as well as to the lower frequency (but higher amplitude) periodic lateral flapping of the jet across the plate. These additional complex unsteady interactions are manifested in the behavior of the time-averaged stagnation Nusselt number (Fig. 7). There is a distinct demarcation between the steady behavior for $Re < 650$ and the unsteady behavior for $Re > 650$. As is also found in laminar-to-turbulent transitions, the dependence of Nusselt number on impinging Reynolds number in the unsteady regime is lessened because the heat transfer is enhanced by the higher-order, non-linear, unsteady mechanisms. In the steady cases, the stagnation Nusselt number is set solely by the magnitude of the steady impinging velocity, which is in direct proportion to the jet Reynolds number. A comparison of representative local instantaneous and time-averaged

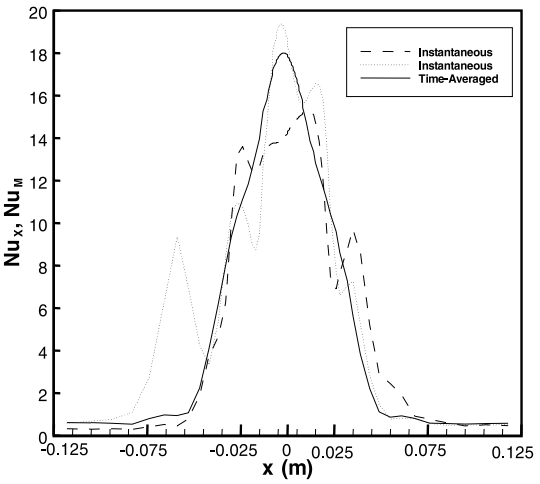

Fig. 14. Time-averaged versus instantaneous Nusselt numbers for $Re = 750$.

Nusselt numbers for $Re = 750$ is shown in Fig. 14. The instantaneous profiles demonstrate several local maxima and severe asymmetry. Averaged over long time, the unsteady contributions to the heat transfer broaden the extent of cooling, compared to the steady cases. The occurrence of the inflection point on the Nu profile and the fuller lobes are indicative of the enhancement of heat transfer due to the unsteady flow. The relative contributions of the various dominant modes are subject to future investigation.

The critical Reynolds number at which the laminar jet demonstrates instabilities leading to the onset of unsteady flow was examined by successively examining spectra of u and v at the three monitoring locations, at

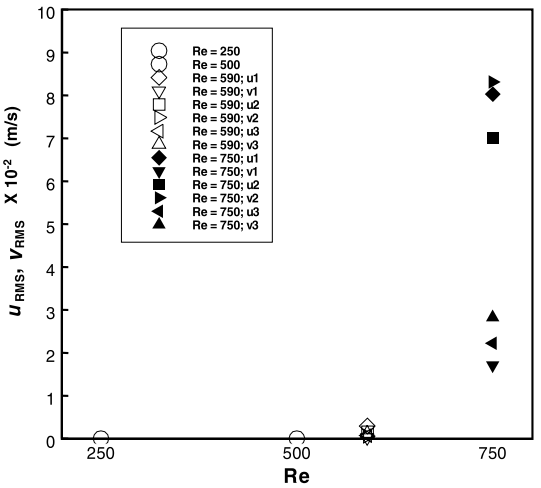

Fig. 15. Root-mean-square for the u- and v-velocities at three monitoring locations.

Reynolds numbers from 500 to 750. The critical Reynolds number was found to be in the vicinity of 585–610, as determined by observation of the Reynolds number at which the root-mean-square average of u and v departs from zero (Fig. 15). The exact value is difficult to identify because numerically induced disturbances may artificially trigger the instability. However, it is safe to assume that the range covers the exact critical Reynolds number.

5. Conclusions

A numerical investigation of the confined impinging jet was performed for Reynolds numbers of 250, 500, and 750, based on hydraulic diameter. Visualization of the numerical simulations showed the complexity of the flow field, steady for Reynolds numbers of 250 and 500 and unsteady for a Reynolds number of 750. Wall pressure, friction, and heat transfer coefficients reached a peak value in the vicinity of the stagnation point for all cases under investigation, as expected. The physical interpretation of the flow field emphasized the impact of varying Reynolds numbers on the heat transfer. At $Re = 250$, separation of the boundary layer developing on the target wall was observed but the separation disappeared at $Re = 500$. For $Re = 250$, the stagnation Nusselt was lower due to the thicker diffusive layer, but the decay rate of Nusselt number in the direction moving away from the stagnation line was lower as the arriving jet was broader in the transverse direction. The time-averaged Nu for $Re = 750$ demonstrated behavior that was indicative of a shift in the flow regime. The peak value was higher but the rate of decay of Nu away from the stagnation line showed an inflection point that broadened the effectively cooled area. At $Re = 750$ the spectral distribution of the velocity in the jet streamwise and spanwise directions at three distinct locations in the jet pointed out three dominant frequencies. The highest frequency is related to the asymmetric vortex shedding, which leads to "buckling" of the jet. The lowest frequency is associated with jet "flapping" or "sweeping" against the target wall. It is thought that the flapping instability results from a non-linear interaction between the jet and the channel fluid. The critical Reynolds number for the onset of unsteady flow is located between 585 and 610, as determined by the observation of the Reynolds number at which the root-mean-square average of u and v departed from zero. The dependence of the Nusselt number on impinging Reynolds number in the unsteady regime is lessened because the heat transfer is enhanced by the non-linear unsteady mechanisms. By comparison, for the steady cases, the stagnation Nusselt number is directly proportional to the jet Reynolds number, depending principally on the velocity magnitude. Averaged over a long time, the unsteady contri-

butions to the heat transfer broaden the extent of cooling, compared to the steady cases.

Acknowledgements

This work would not have been possible without the dedicated efforts of our colleagues, Dr. Jorge Luis Rosales and Prof. J.A.C. Humphrey, in developing the FAHTSO code. We are grateful to them for their many contributions to this study.

References

[1] D. Lytle, B.W. Webb, Air jet impingement heat transfer at low nozzle–plate spacing, Int. J. Heat Mass Transfer 37 (1993) 1687–1697.
[2] L. Huang, M.S. El-Genk, Heat transfer of an impinging jet on a flat surface, Int. J. Heat Mass Transfer 37 (1993) 1915–1923.
[3] M. Kurosaka, M.D. Fox, L. Hedges, K. Hirano, The influence of vortical structures on the thermal fields of jets, J. Fluid Mech. 255 (1993) 447–472.
[4] S.L. Anderson, E.K. Longmire, Particle motion in the stagnation zone of an impinging jet, J. Fluid Mech. 299 (1995) 333–366.
[5] J.A. Fitzgerald, S.V. Garimella, Flow field effects on heat transfer in confined jet impingement, Trans. ASME, J. Heat Transfer 119 (1997) 630–635.
[6] S.V. Garimella, R.A. Rice, Confined and submerged liquid jet impingement heat transfer, Trans. ASME, J. Heat Transfer 117 (1995) 871–877.
[7] G. Morris, S.V. Garimella, Prediction of jet impingement heat transfer using a hybrid wall treatment with different turbulent Prandtl number functions, Trans. ASME, J. Heat Transfer 118 (1996) 562–569.
[8] J.L. Rosales, A numerical investigation of the fluid and heat transfer in unsteady viscous flow past square cylinders, Ph.D. Thesis, University of Arizona, Tucson, Arizona, 1999.
[9] V.A. Chiriac, The numerical investigation of the unsteady flow field and heat transfer in a laminar forced and unforced confined impinging jet, Ph.D. Thesis, University of Arizona, Tucson, Arizona, 1999.
[10] S.V. Patankar, Numerical Heat Transfer and Fluid Flow, Hemisphere, McGraw-Hill, New York, 1980.
[11] T. Hayase, J.A.C. Humphrey, R. Greif, A consistently formulated QUICK scheme for fast and stable convergence using finite-volume iterative calculations procedures, J. Comp. Phys. 98 (1992) 108–118.
[12] J.P. Wheeler, S. Neti, Heat transfer for a semi-confined impinging laminar jet, in: 1999 National Heat Transfer Conference, Albuquerque, New MexicoTrans. ASME (1999).